PHYSICS OF FLUIDS **25**, 072102 (2013)

Simulations of the breakup of liquid filaments on a partially wetting solid substrate

Giovanni Ghigliotti,[1] Chunfeng Zhou,[2] and James J. Feng[1,3]
[1]*Department of Mathematics, University of British Columbia, Vancouver, British Columbia V6T 1Z2, Canada*
[2]*Corning Incorporated, One Science Center Drive, Corning, New York 14831, USA*
[3]*Department of Chemical and Biological Engineering, University of British Columbia, Vancouver, British Columbia V6T 1Z3, Canada*

(Received 23 August 2012; accepted 12 June 2013; published online 1 July 2013)

We report direct numerical simulations of liquid filaments breaking up into droplets on partially wetting substrates. It is motivated by recent experiments, linear stability analyses, and lubrication-based calculations. The fluid flow is governed by the Stokes equations and the contact line motion is handled by a phase-field model, which also serves to capture the interfacial motion. The coupled Stokes and Cahn-Hilliard equations are solved using a finite-element algorithm in three dimensions. This avoids additional approximations of the fluid flow or contact line motion, and allows us to compute arbitrary contact angles on the substrate. We simulate both the breakup of infinite liquid filaments via growing capillary waves and that of finite liquid filaments with drops pinching off from the ends, with a focus on the effect of the wetting angle. In both cases, substrate hydrophobicity promotes breakup of the thread, and decreases the spacing of the daughter drops. The results show the differences in the two processes and in the final drop size and spacing. The development of capillary waves agrees well with prior linear analysis and the end-pinching results offer new insights into this poorly understood phenomenon. © *2013 AIP Publishing LLC*. [http://dx.doi.org/10.1063/1.4812252]

I. INTRODUCTION

Consider a uniform liquid filament on a smooth and homogeneous substrate, on which the liquid makes a contact angle θ. Under the action of capillarity, the filament may break up into droplets through one of two mechanisms. If the thread is thin and long, with a large aspect ratio, its bulk does not feel the effect of the ends, and the thread breaks up through the counterpart of the Rayleigh-Plateau instability.[1] Capillary waves develop on the filament with periodic necking along the axial direction while the contact line shifts accordingly. These waves modulate the mean curvature of the liquid surface and generate gradients of the Laplace pressure, which further amplify the perturbation till breakup.[2–4] For brevity, we will refer hereafter to this breakup mechanism as the *capillary wave* breakup, but not to be confused with that on a freely suspended filament. Note that this is not limited to infinitely long straight filaments; Wu *et al.*[5] studied capillary wave development on a ring, thereby avoiding the tips altogether.

The second mechanism, *end-pinching* or pearling, prevails on filaments of relatively small aspect ratio. Similar to its counterpart on free filaments,[6] the tip retracts because of surface tension, collecting the liquid into a bulb. Negative axial curvature at the base of the bulb creates a minimum pressure that induces a converging flow, generating a neck on the side away from the bulb. The increased azimuthal curvature at the neck increases the pressure locally and drives the fluid toward the end, leading eventually to pinch-off.[7] The process repeats until the entire filament is broken up.[8] If the filament is too short, end-pinching may not have time to develop before the entire thread shrinks into a sessile drop.

Although the capillary wave breakup resembles that of a free filament, the moving contact line renders the theoretical analysis much more difficult. Using an energetic approach and various slip models for the contact line, Davis[2] analyzed the linear instability of infinitely long rivulets in the absence of gravity. Brochard-Wyart and Redon[3] used a simplified energetic formulation to study the coupling of the motion of the two contact lines for an arbitrary contact angle. By using two different slip models, Yang and Homsy[4] solved the flow field in the filament for contact angles $\theta \leq \frac{\pi}{2}$, obtaining the dispersion relations for the capillary waves. McCallum *et al.*[9] developed an analytical model that assumes a diffusion equation for the fluid interface. It allows an arbitrary contact angle, but does not solve the velocity field in the filament and is thus limited to qualitative results. Diez *et al.*[10–12] developed two theories based, respectively, on a precursor-film model and a slip model for the contact line, and also allowed gravity to deform the shape of the filament. Yang and Homsy[4] and Diez *et al.*[10,11] both used the lubrication approximation to reduce the free-surface Stokes equations to a single partial differential equation governing the height of the filament. Both groups also carried out numerical solutions of the lubrication equation to study the nonlinear growth of the instability. Molecular dynamics simulations have also been performed on nanoscopic filaments.[13]

For end-pinching, the few theoretical and numerical studies that we are aware of have used the precursor-film model.[10,11,14] They predict formation and pinch-off of droplets from the ends, but the drop size and spacing correspond to the wavelength of the fastest capillary wave mode, and are smaller than the experimental values. Diez *et al.*[10] attributed these discrepancies to "intrinsic limitations of this lubrication approach." Furthermore, the precursor model with a van der Waals disjoining potential does not accurately capture the width of macroscopic filaments, and cannot accommodate moderately large contact angles.[10] On the last point, the lubrication approximation and precursor film model are supposed to fail for large contact angles in any event.

So far, experiments have focused on the spacing between the sessile droplets that are produced by either type of instability. In both cases, results suggest that the droplets will be more closely spaced for larger contact angles.[5,8,14] This trend has been predicted by analytical and semi-analytical models for the growth of capillary waves,[4,11] but for end-pinching there has been no theoretical study. Generally, lubrication analysis with a slip or precursor model at the contact lines gives reasonably good predictions for small-scale filaments or small contact angles,[12,14] but not for larger contact angles and thicker filaments.

Thus, it appears worthwhile to carry out numerical simulations of the two capillary instabilities—capillary wave growth and end-pinching—without the lubrication approximation, and with a more sophisticated contact line model. The objective of this study is to characterize the two capillary instabilities in the breakup of a substrate-bounded liquid filament in full three dimensions. We achieve this through a diffuse-interface model. By solving the Stokes equations coupled with Cahn-Hilliard dynamics at the interface, we go beyond the limitations in prior theoretical analysis. The results shown here give quantitative predictions of the dynamics and final configurations for the two capillary instabilities of a liquid filament for a wide range of contact angles.

II. THEORY AND NUMERICAL METHOD

Our algorithm AMPHI, standing for Adaptive Meshing for Phase Field (ϕ), uses a diffuse-interface model and a fully implicit finite-element solver on unstructured grids.[15] The interface is viewed as a diffuse transition layer of small but finite thickness, and the diffusion of the two components in this layer is described by the Cahn-Hilliard model. This formalism not only provides a means for interface capturing, via the phase field ϕ, but also naturally regularizes the singularity at the moving contact line. The 2D and 3D versions of AMPHI have been described in detail elsewhere, along with comprehensive validations, especially with regard to the convergence of the diffuse-interface model toward a sharp-interface limit.[15–17] For completeness, we outline the theoretical model and the numerical method in the following.

Consider immiscible fluids F_1 and F_2 in contact with each other and with a solid wall W. We define the phase-field variable ϕ such that the concentrations of the two fluid components are $(1+\phi)/2$ and $(1-\phi)/2$, respectively. Then ϕ takes on a value of 1 or -1 in the two bulk phases, and the interface is simply the level set $\phi = 0$. The interactions among F_1, F_2, and W are represented

by three interfacial tensions: σ between F_1 and F_2, and σ_{w1} and σ_{w2} for the fluid-wall interaction. In the diffuse interface framework, σ is represented by a mixing energy inside the diffuse interface. Starting with the system's free energy, we arrive at the following governing equations:[15]

$$\frac{\partial \phi}{\partial t} + \boldsymbol{v} \cdot \nabla \phi = \nabla \cdot (\gamma \nabla G), \tag{1}$$

$$G = \lambda \left[-\nabla^2 \phi + \frac{\phi(\phi^2 - 1)}{\epsilon^2} \right], \tag{2}$$

$$0 = -\nabla p + \nabla \cdot \left[\mu \left(\nabla \boldsymbol{v} + (\nabla \boldsymbol{v})^T \right) \right] + G \nabla \phi, \tag{3}$$

$$\nabla \cdot \boldsymbol{v} = 0, \tag{4}$$

where G is the chemical potential and γ is the mobility parameter; λ is the interfacial energy density and the capillary width ϵ represents the interfacial thickness. $\boldsymbol{v}$ is velocity and p is pressure. Since the process to be simulated is slow, we neglect inertia in the momentum equation and will solve the coupled Stokes-Cahn-Hilliard system. Besides, we neglect gravity. For common fluids, the capillary length is on the order of 1 to several millimeters.[8] Neglecting gravity thus limits us to filaments thinner than 1 mm in diameter. To a degree, this detracts from the advantage of the phase-field model over prior lubrication models in simulating thicker filaments. But we have accepted the limitation for the simplification that it brings to analyzing the data. With decreasing ϵ, the diffuse-interface model approaches the classical sharp-interface model and $\frac{2\sqrt{2}}{3}\frac{\lambda}{\epsilon}$ gives the interfacial tension σ.[18] μ is the mixture viscosity defined by algebraic averaging of the component values: $\mu = \frac{1+\phi}{2}\mu_1 + \frac{1-\phi}{2}\mu_2$.

The governing equations are supplemented by the following boundary conditions on the domain boundary $\partial\Omega$:

$$\boldsymbol{v} = \boldsymbol{u}, \qquad \text{on } (\partial\Omega)_u, \tag{5}$$

$$(-p\boldsymbol{I} + \boldsymbol{\tau}) \cdot \boldsymbol{n} = 0, \qquad \text{on } (\partial\Omega)_\tau, \tag{6}$$

$$\boldsymbol{n} \cdot \nabla G = 0, \qquad \text{on } \partial\Omega, \tag{7}$$

$$\boldsymbol{n} \cdot \nabla \phi = 0, \qquad \text{on } \partial\Omega \setminus (\partial\Omega)_w, \tag{8}$$

$$\boldsymbol{n} \cdot \nabla \phi = -\frac{1}{\lambda} f_w'(\phi), \qquad \text{on } (\partial\Omega)_w, \tag{9}$$

where $(\partial\Omega)_u$ and $(\partial\Omega)_\tau$ are portions of $\partial\Omega$ having velocity and stress conditions: $\partial\Omega = (\partial\Omega)_u \bigcup (\partial\Omega)_\tau$ and $(\partial\Omega)_u \bigcap (\partial\Omega)_\tau = \emptyset$, and $(\partial\Omega)_w$ is the solid wall. $\boldsymbol{n}$ is the unit normal to the boundary and $\boldsymbol{u}$ is the boundary velocity. Equation (5) is the no-slip boundary condition, which implies that the motion of the contact line is solely due to the Cahn-Hilliard diffusion. Equations (7) and (8) impose zero flux through the boundaries and conserve mass for each fluid component. In Eq. (9), f_w is the wall energy in diffuse-interface form:[17,19,20]

$$f_w(\phi) = -\sigma \cos\theta \frac{\phi(3 - \phi^2)}{4} + \frac{\sigma_{w1} + \sigma_{w2}}{2}, \tag{10}$$

and the fluid-fluid and fluid-solid interfacial tensions determine the static contact angle θ through Young's equation:

$$\sigma \cos\theta = \sigma_{w2} - \sigma_{w1}. \tag{11}$$

For the simplest case of a constant $f_w = \sigma_{w1} = \sigma_{w2}$, the static contact angle $\theta = \frac{\pi}{2}$ and the two fluid components are neutrally wetting on the solid substrate. Other contact angles are specified by a non-constant $f_w(\phi)$.

The mesoscopic contact line model described here enjoys some advantages over previous models.[17,21,22] In a sense, it coarse-grains microscopic physics into interfacial energies, and integrates these energies into macroscopic fluid dynamics. On the one hand, it captures the local features of the Cox solution.[17] On the other, it is amenable to large-scale flow computations as in the present paper. The phase field not only regularizes the contact line singularity, but also serves as a computational device for interface capturing. An additional benefit, important in the current context, is the ability to simulate interfacial breakup in a natural way.[23] The interfacial energy produces a short-range force between interfaces akin to the van der Waals force.[24,25] Note that Eq. (9) amounts to assuming the ϕ field being at equilibrium with the solid substrate. As a result, the dynamic contact angle remains at the static value up to first order in the capillary number.[17] This aspect resembles the "fixed contact angle model" used by Davis[2] and Yang and Homsy.[4] However, our model differs from theirs in a way that we do not have "perfect slip." In fact, the dissipation at the contact line consists of viscous friction and an additional contribution due to Cahn-Hilliard diffusion.[15]

The above equations are discretized using the Galerkin formulation on a 3D unstructured tetrahedral finite-element mesh. An adaptive meshing scheme has been used to accurately resolve the interface at moderate computational costs.[16] Typically the interfacial layer requires roughly 10 grid points to resolve, and remeshing happens every tens of time steps. We use implicit time-stepping, with Newton iteration at every step to handle the nonlinearity in the equations. Numerical experiments with grid refinement have been carried out,[16] and adequate resolution is ensured for the simulations presented in the following.

From the cross-sectional area A of the filament, we define an effective radius $R = \sqrt{\frac{2A}{\pi}}$ and use it as the characteristic length. The characteristic time scale is the capillary time $\tau_c = \frac{\mu_1 R}{\sigma}$, μ_1 being the viscosity of the filament liquid. The only macroscopic dimensionless parameter of the problem is the filament-to-medium viscosity ratio $\beta = \frac{\mu_1}{\mu_2}$. The phase field model introduces two additional dimensionless numbers: the Cahn number Cn and the Péclet number Pe:

$$Cn = \frac{\epsilon}{R}, \tag{12}$$

$$Pe = \frac{\sigma R \epsilon^2}{\mu_1 \gamma \lambda} \equiv \frac{2\sqrt{2}}{3} \frac{R\epsilon}{\mu_1 \gamma}. \tag{13}$$

Cn indicates the thickness of the diffuse interface, and should be small enough to achieve the sharp interface limit.[16,17] Pe reflects the magnitude of Cahn-Hilliard diffusion. It is in principle material-specific, and should be determined by fitting the speed of the contact line in specific experiments.[17,26–28] Zhou *et al.*[16] have studied drop spreading on a partially wetting substrate using the current AMPHI algorithm. They found that $Pe \sim 5000$ gives reasonable agreement with the experiment by Zosel.[29] For simulating the growth of capillary waves on an infinite filament, we have used $Cn = 0.05$ and $Pe = 4714$. A convergence test shows that this Cn accurately reproduces the perturbation growth rate to within 2%. The Pe value is not meant to correspond to a particular experiment. Moreover, numerical experiments show the results to be relatively insensitive to Pe. For example, the growth rate of the capillary waves increases by less than 10% when Pe increases from 471.4 to 4714. Simulating end-pinching requires a larger computational domain, and we have used a larger interface thickness so that $Cn = 0.1$ and $Pe = 9428$. The effect of these values will be discussed in Subsection III B.

III. RESULTS AND DISCUSSION

In the following we consider two different setups: an infinite liquid filament for simulating the growth of capillary waves and a finite filament of moderate length for simulating end-pinching. In the context of wall-bounded liquid filaments, these appear to be the first solutions of the fully three-dimensional equations of motion for a liquid filament. An appealing feature of our model is the ability to accommodate arbitrary contact angles. By interrogating the numerical solutions and comparing with existing results where possible, we explore the following fundamental questions: What is the effect of the contact angle on the capillary instabilities of a liquid filament? How do the

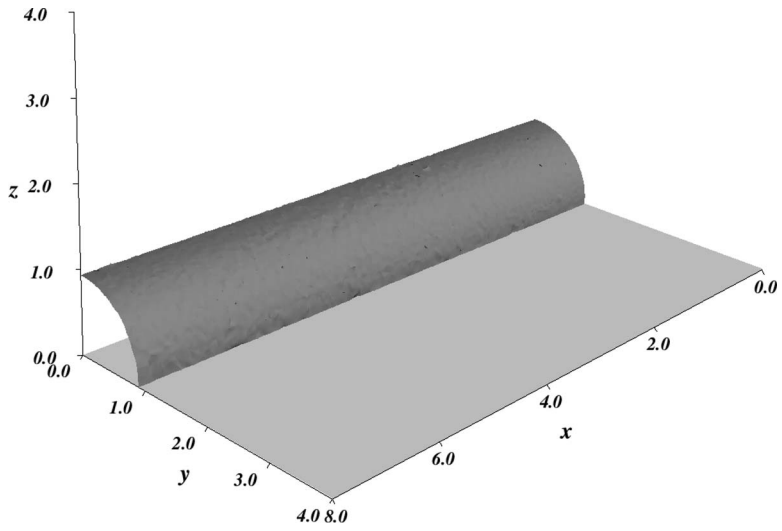

FIG. 1. A schematic of the computational domain. Symmetry in the x and y directions is exploited to reduce the computational cost.

size and spacing of the sessile drops differ for the two instability mechanisms? For what filament length, contact angle, and viscosity contrast can end-pinching take place?

A. Capillary waves

We consider a fluid filament of infinite length on a substrate, which forms the bottom of the computational domain ($z = 0$ in Fig. 1). The filament has a circular cross-section that accommodates the static contact angle with the substrate. The computational domain consists of a rectangular box of length L, width W, and height H, with a filament spanning the whole length L in the x direction. Due to the symmetry of the problem in the transverse y direction (parallel to the substrate and normal to the axial x direction), only half of the filament is computed in the simulations, as showed in Fig. 1.

Symmetry conditions are applied on the planes $x = 0$, $x = L$, and $y = 0$. We use impermeability (Eq. (7)) and no-slip conditions on the substrate, and the stress-free condition on the top ($z = H$) and side ($y = W$) of the computational domain. At the start, a sinusoidal perturbation is applied to the surface of the filament:

$$r = r_0 + a_0 \cos\left(\frac{\pi x}{L}\right), \tag{14}$$

with $a_0 = 0.01R$ being the initial amplitude of the perturbation, and $r_0 = \sqrt{\frac{\pi}{2\theta - \sin 2\theta}}R$ is the radius of the circular cross section. Note that the imposed perturbation has a wavelength $\Lambda = 2L$, and only half of the wave is computed in the simulations, thanks to the symmetry conditions at $x = 0$ and $x = L$. L is varied to impose different wavelengths with the corresponding wave number $k = \frac{2\pi}{\Lambda} = \frac{\pi}{L}$. W and H values range between $3R$ and $5R$, large enough not to affect the results with numerical confinement. The contact angle θ, uniform over the substrate, is varied between $\pi/4$ and $5\pi/6$. The viscosity ratio β is chosen to be 50, roughly corresponding to the water-air viscosity ratio. Numerical experimentation shows that for $\beta \geq 30$, the ambient viscosity becomes negligible and β no longer affects the results.

Figure 2 shows snapshots of a typical example of the capillary wave growth and the resultant breakup. The primary neck remains at $x = L$ until $t = 300$, after which a secondary neck develops in the middle, where breakup eventually occurs. As a result, a primary droplet forms at $x = 0$, location of the initial bulge, while a secondary drop forms at $x = L$, location of the initial valley. The secondary drop has a volume roughly 0.8% of that of the primary one.

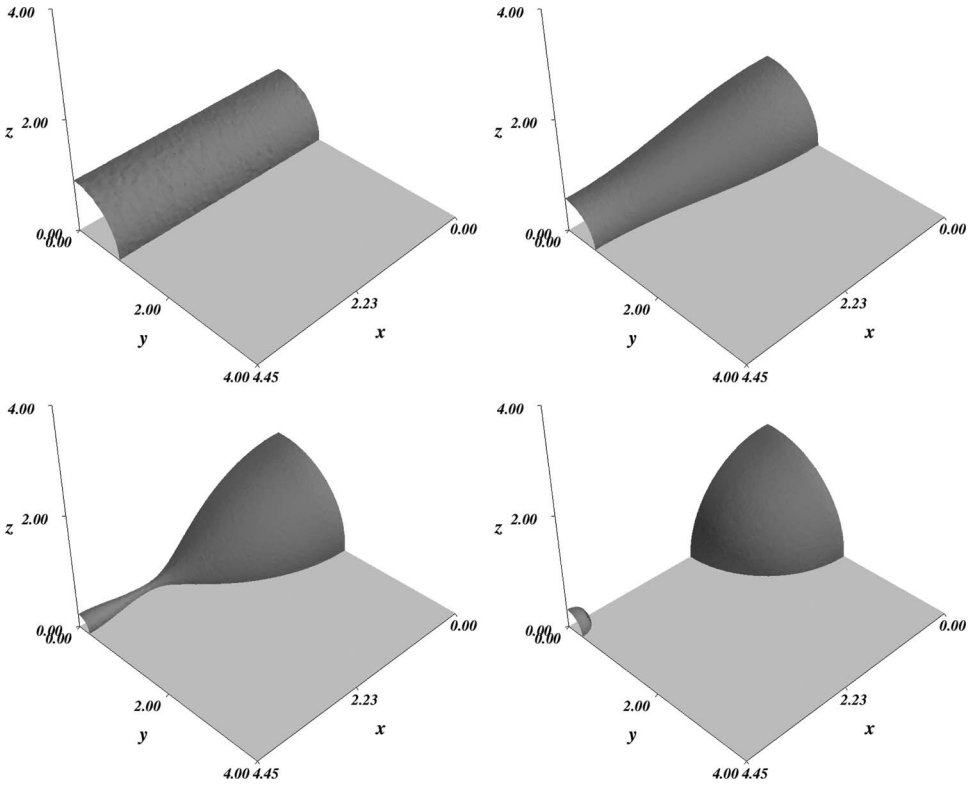

FIG. 2. Capillary wave growth: snapshots at times $t = 0$, 300, 400, and 600, with $\Lambda = 8.9$ and $\theta = \frac{\pi}{2}$.

Linear theories[4,10] predict an initial linear regime in which the amplitude of the imposed sinusoidal perturbation grows exponentially while the shape of the contact line remains sinusoidal. We adopt a similar approach and fit the contact line position with a sinusoidal function, and plot its amplitude in Fig. 3 as a function of time. The amplitude a of the perturbation grows exponentially as expected, and then saturates towards a value close to the effective radius of the filament as breakup commences. The perturbation is found to be approximately sinusoidal up to $t \approx 300$. The breakup happens at $t \approx 400$. These times, of course, depend on the initial amplitude of the perturbation.

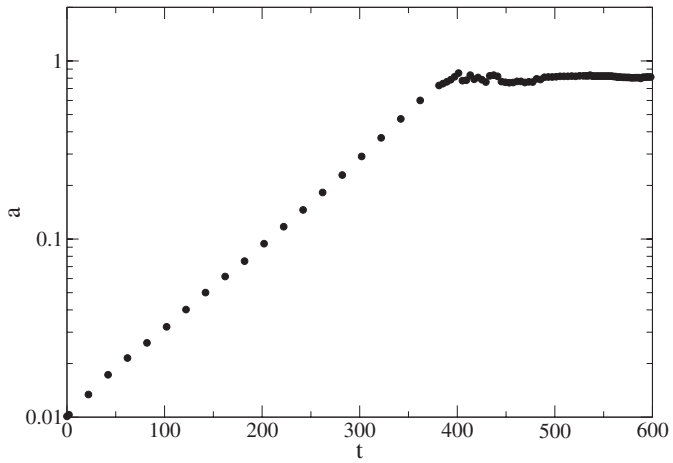

FIG. 3. Growth of the amplitude of the perturbation in time. $\Lambda = 8.9$ and $\theta = \frac{\pi}{2}$.

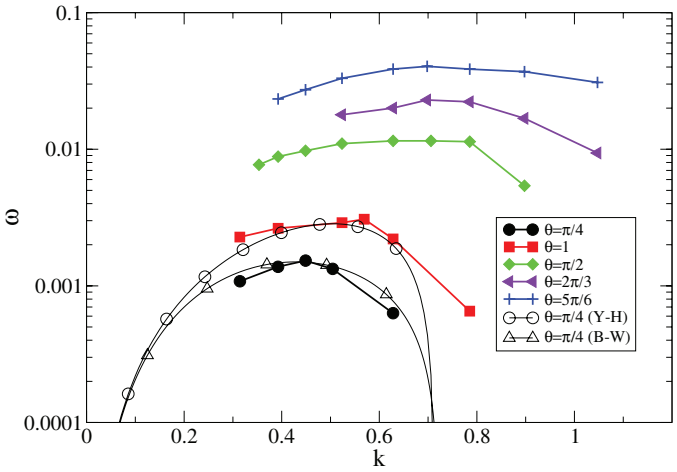

FIG. 4. Dispersion relation for the capillary waves on the surface of a liquid filament for different values of the contact angle θ. The theoretical results of Yang and Homsy[4] (Y-H) and Brochard-Wyart and Redon[3] (B-W) are also plotted for comparison, the latter having an indeterminate prefactor that is fitted to our curve.

Figure 4 plots the dispersion relation computed for five contact angles with the growth rate ω determined from the amplitude $a(t) = a_0 e^{\omega t}$ as plotted in Fig. 3. The general trend is that hydrophobicity facilitates the growth of the capillary waves. With increasing θ, the critical wavenumber and the fastest growing wavenumber both shift to shorter waves with the maximum growth rate increasing by a factor of 30 from $\theta = \frac{\pi}{4}$ to $\theta = \frac{5\pi}{6}$. This can be rationalized from two factors. First, a larger contact angle produces a higher azimuthal curvature, which is the motor driving the instability.[4] This shifts the balance between the gradients of azimuthal and axial curvatures in favor of the former, thereby destabilizing the filament. Second, a higher contact angle corresponds to a smaller contact area with the substrate, and thus a lower viscous dissipation during the breakup. Both promote the growth of the capillary waves.

We compare our dispersion relations with those predicted by the theories of Yang and Homsy[4] and Brochard-Wyart and Redon[3] for $\theta = \frac{\pi}{4}$ (Fig. 4). The model of Yang and Homsy applies for contact angles $\theta \leq \frac{\pi}{2}$, as they require the height of the surface to be a single-valued function of the horizontal position on the substrate, and $\theta = \frac{\pi}{4}$ is the only value for which the growth rates are reported. In comparing our $\theta = \frac{\pi}{4}$ curve with theirs, we note very similar shapes but their growth rate is greater by a factor close to 2. A probable cause for this discrepancy is their use of a *perfect slip* condition at the contact line. In our model, the contact line sustains a viscous dissipation due to Cahn-Hilliard diffusion.[15] We know of no experimental data on the temporal evolution of the instability that would allow a quantitative check of the predicted growth rates.

The model by Brochard-Wyart and Redon[3] predicts the following dispersion relation:

$$\omega^{BW} \sim \theta^3 \frac{k}{1 + \frac{1}{k^2 r_0^2 \sin^2\theta}} \left[\tanh(k r_0 \sin\theta) - \frac{1}{k r_0 \sin\theta} \right], \tag{15}$$

where $r_0 = \sqrt{\frac{\pi}{2\theta - \sin(2\theta)}} R$ is the initial radius of curvature of the filament.[30] The amplitude is specified modulo an undetermined constant prefactor related to the contact line singularity, independent of θ. We have fixed this prefactor by equating ω^{BW} to our prediction for an intermediate wavenumber, and plotted the dispersion relation in Fig. 4. There is close agreement between the two.

We compare the fastest growing modes with the ones predicted by the theories of Yang and Homsy[4] and of Brochard-Wyart and Redon[3] in Fig. 5. The agreement with Yang and Homsy's predictions is very good, with only a 10% discrepancy on the fastest wavelength for the smallest contact angle $\theta = \frac{\pi}{4}$. This discrepancy may be due to the excessive Cahn-Hilliard interfacial diffusion in our model, especially for slow growth that occurs at small contact angles. Brochard-Wyart and Redon[3] also predict a fastest wavenumber that increases with the contact angle. However, for

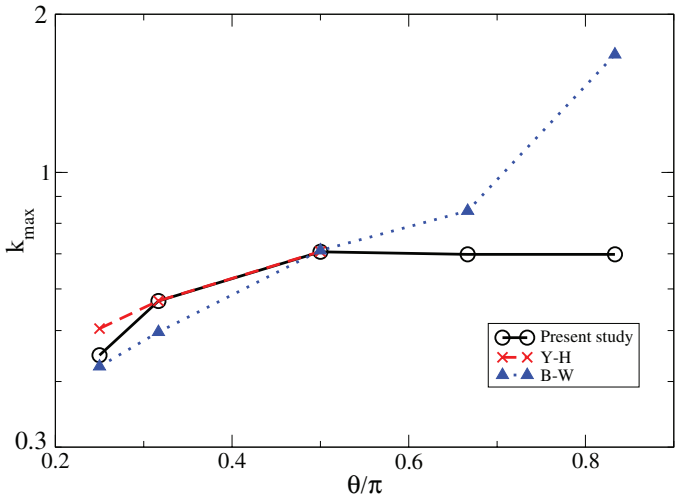

FIG. 5. The fastest growing mode for different values of the contact angle θ: comparison between our simulation and prior theoretical predictions.

$\theta \to \pi$, their k_{max} diverges. This destabilization of infinitely short waves does not seem physically reasonable, and is absent from our computation. It is worth noting that as $\theta \to \pi$, the dynamics of the filament does not approach that of a free filament, since the presence of the contact line constrains the perturbation to be non-axisymmetric.[31]

We turn now to the nonlinear regime of capillary wave growth. In our simulations, the linearly dominant wavelength always persists till the end. What is not predicted by the linear theories is the appearance of a secondary neck, which causes the formation of a secondary droplet. In fact, in all the cases considered, we obtained a secondary drop in the primary neck region ($x = 0$, Fig. 2). This is in agreement with previous numerical and experimental results.[4,8] Yang and Homsy[4] obtained tertiary droplets and inferred the existence of an infinite cascade of drop formations. In our simulations, the diffuse nature of the interface imposes a lower cutoff length-scale $\sim Cn$. Thus, we are unable to resolve smaller tertiary drops.

Carrying out the fastest mode till breakup, we examine in Fig. 6 the variations of the primary drop spacing d (measured center-to-center) and secondary drop size V_s with the contact angle θ.

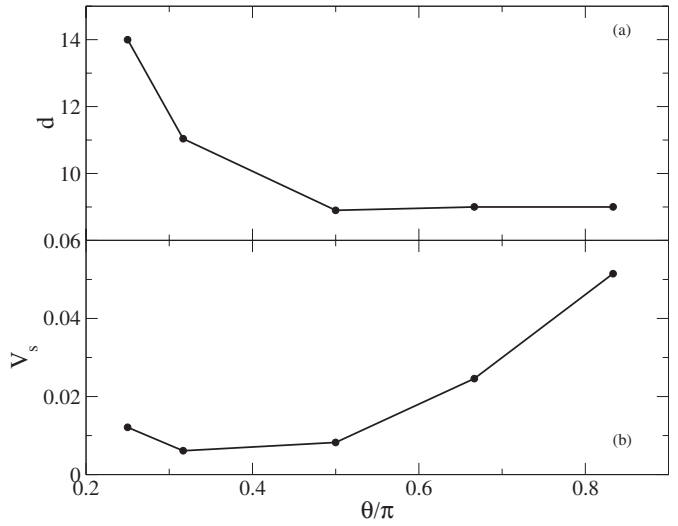

FIG. 6. (a) Center-to-center distance d between primary drops and (b) volume V_s of secondary drops as functions of θ for the fastest mode. V_s is normalized by the volume of the primary drops.

As noted above, the spacing between the primary drops corresponds exactly with the wavelength of the linearly most dangerous mode, and this decreases with θ initially and then levels off. Our d values are consistent with experimental observations of Wu *et al.*[5] ($d = 14 \pm 4$ for $\theta \simeq 0.28\pi$) and Kondic *et al.*[14] ($d \simeq 14 \pm 5$ for $\theta > \frac{\pi}{2}$). A more definitive comparison is thwarted by experimental complications that produce a high level of polydispersity. For the lower contact angles, the secondary droplet has a volume of only around 1% of that of the primary drops. But this ratio increases to about 5% for $\theta = 5\pi/6$. This may be due to the increased growth rate of the fastest mode at higher θ, which leaves a shorter time for the fluid to drain from the neck into the primary drop. These results suggest that the contact angle can be used to control drop size and spacing in microfluidic devices. For example, one may use electrowetting to generate arrays of equally spaced drops with a controlled bidispersity by using contact angles $\frac{\pi}{2} \leq \theta \leq \pi$.

B. End-pinching

For a finite-length liquid filament, we assume fore-aft symmetry between the two halves and thus simulate only one quarter of the filament (Fig. 7). Symmetry conditions are applied on the planes $x = 0$ and $y = 0$ (right and back faces of the computational box). On the substrate (bottom, $z = 0$) we use impermeability and no-slip conditions, and on the three remaining planes we apply the stress-free condition. Such a filament of finite length is not an equilibrium configuration due to Laplace pressure in the tips that drives retraction. To be definite and uniform, all the filaments are initialized with a circular cross section and a spherical cap on the tip, both of radius R. The initial contact angle is equal to $\frac{\pi}{2}$ all along the contact line, regardless of the equilibrium contact angles θ. This incurs a fast initial relaxation toward the proper θ, which has little impact on the ensuing end-pinching.

While the experiments employed liquid filaments of initial length $\zeta \sim 100$ or higher,[8,14] computational cost limits us to shorter filament of length up to $\zeta \approx 40$. Here, ζ is measured from the tips of the liquid filament in the initial configuration and scaled by R. Within the parameter range we have explored, two general behaviors have been observed. Shorter filaments (ζ below a critical length ζ_c) retract into a single sessile drop without breaking up at all. Longer ones, with $\zeta \geq \zeta_c$, break up at the center of the filament forming two primary droplets (Fig. 7). It turns out that ζ_c depends on the contact angle θ and the viscosity ratio β. In the following, therefore, we will examine the critical length ζ_c and the spacing between daughter drops as functions of θ and β.

To keep the computational cost manageable, we have used a larger interface thickness $\epsilon = 0.1R$ for this section, so that $Cn = 0.1$ and $Pe = 9428$. Numerical experiments show that this hardly affects ζ_c and the spacing of the daughter drops. For three contact angles $\theta = 1$, $\frac{\pi}{2}$, and $\frac{2\pi}{3}$, we have tested $\epsilon = 0.05$, 0.075, and 0.1, and found the drop spacing to vary within 3%. No variation in ζ_c

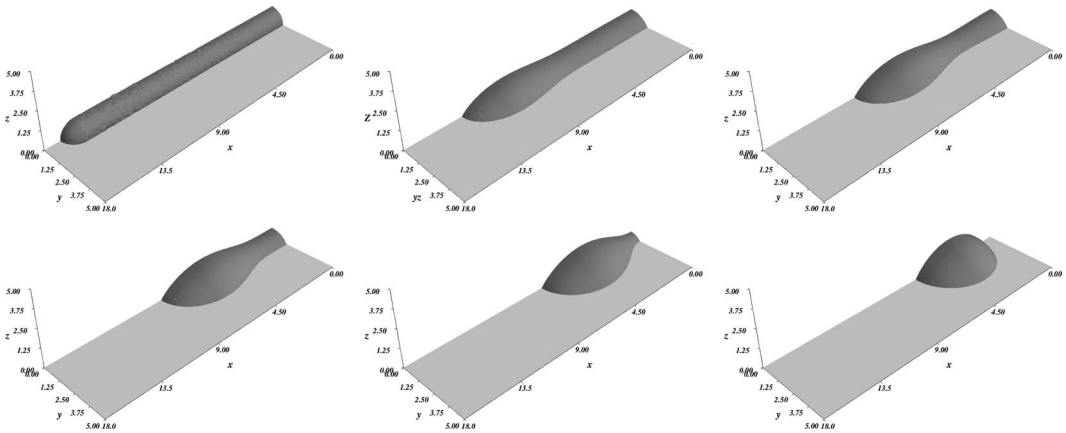

FIG. 7. End-pinching generating two primary droplets. Note that only a quarter of the filament is shown for symmetry. The snapshots are at times $t = 0$, 285, 585, 885, 1185, and 1785. $\theta = 1$, $\zeta = 34$, $\beta = 10$.

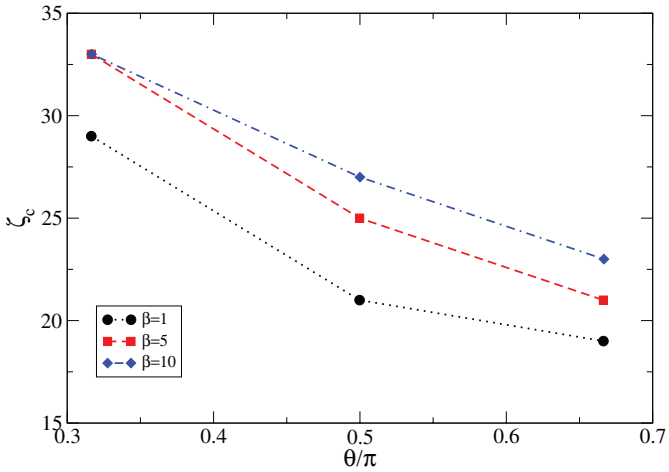

FIG. 8. The critical length of the filament for breakup as a function of the contact angle θ and viscosity ratio β.

was detected when changing ζ by increments of 0.5; its variation is thus at most 2.6% in view of the ζ_c values in Fig. 8. But Cn does affect the speed of the contact line motion and the timescale of the breakup. As an example, for $\theta = \frac{\pi}{2}$ and $\zeta = \zeta_c$, the pinch-off time, defined as the time interval from the applied perturbation to the moment of breakup, is 15% longer for $Cn = 0.1$ than for $Cn = 0.05$, while the drop spacing differs only by 1%.

Figure 8 depicts ζ_c as a function of the viscosity ratio β and contact angle θ. Two general trends are notable. First, ζ_c increases with β within the range tested. In increasing $\beta = \frac{\mu_1}{\mu_2}$, we have kept Pe constant (Eq. (13)). This amounts to reducing μ_2, the viscosity of the external fluid, while keeping the filament viscosity μ_1 fixed. The outer fluid being less viscous, the retraction of the filament is accelerated, and this leaves less time for the necking and breakup to occur. The increase in ζ_c can thus be rationalized. Second, ζ_c tends to decrease with θ. On the one hand, hydrophobicity facilitates the formation of the bulge at the tip and the pinch-off. On the other hand, it also makes for a faster retraction due to decreased dissipation along the substrate. The former apparently has an upper hand.

Figure 8 also suggests a limit as $\theta \to \pi$, when the wetted area under the filament shrinks to a line. In this process, one expects the filament to become increasingly unstable with end-pinching occurring on shorter and shorter filaments. However, it is interesting to contrast such a limit to end-pinching on a *freely suspended* filament, for which Ha and Leal[32] reported a much longer $\zeta_c \approx 66 \pm 10$ for $\beta = 1$. As noted before,[31] a thin solid wire lining the side of the filament changes its dynamics profoundly. By imposing a vanishing velocity on it and suppressing axisymmetric modes, the wire greatly delays the retraction of the end toward the central filament, thus promoting necking and pinch-off. On a free filament, by contrast, a bulging end can stay connected through a thin neck, and can eventually rejoin the main filament without pinch-off. Such a scenario is shown in Fig. 2 of Ha and Leal.[32]

The discussion above may give the impression of a dichotomy between breakup and non-breakup. But there is more subtlety to the picture. A third scenario may arise for certain parameters when pinch-off occurs off the midpoint of the thread and leads to three primary drops (Fig. 9). To explore this behavior, it is useful to refer to a similar phenomenon during the retraction of freely suspended filaments. In this case, Ha and Leal[32] discovered that for certain values of the viscosity ratio, there exist not one but three critical ζ values, ζ_c, $\zeta_c^{(1)}$, $\zeta_c^{(2)}$, so that for $\zeta_c \le \zeta \le \zeta_c^{(1)}$ the filament breaks up into two droplets, for $\zeta_c^{(1)} \le \zeta \le \zeta_c^{(2)}$ no breakup happens at all, and for $\zeta \ge \zeta_c^{(2)}$ the filament breaks up into three or more droplets. The non-breakup for $\zeta_c^{(1)} \le \zeta \le \zeta_c^{(2)}$ is related to the interaction of the two necks forming behind each bulged end of the filament: if the necks are too close to each other, the two fluid streams going from the pinching necks towards the center of the filament will slow each other down and hamper further thinning of the neck and the pinch-off.[7] Guided by this insight, we searched for multiple critical ζ values in our wall-bounded filament, and

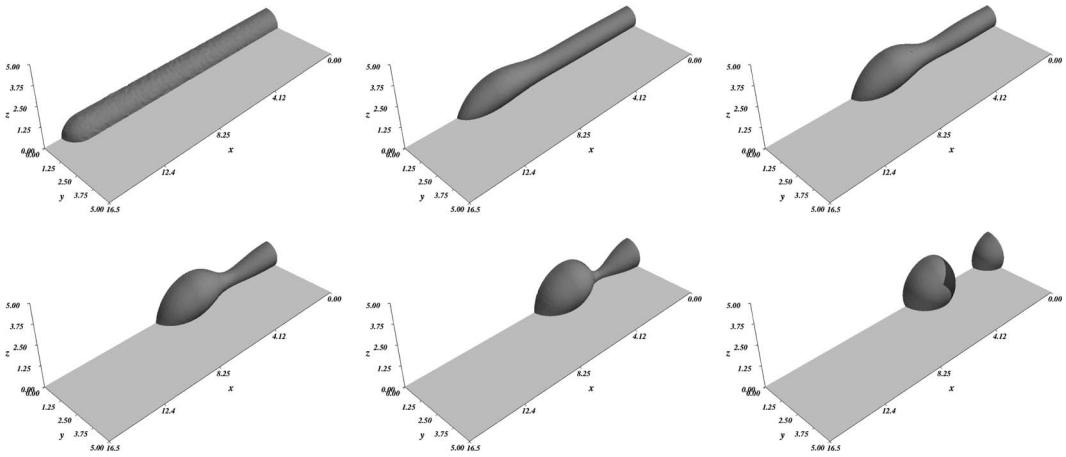

FIG. 9. End-pinching leads to three primary droplets for $\theta = \frac{2\pi}{3}$, $\zeta = 32$, $\beta = 10$. The snapshots are at time $t = 0$, 50, 100, 150, 200, and 300.

indeed found them. For $\theta = \frac{2\pi}{3}$ and $\beta = 10$, we found $\zeta_c = 22$, $\zeta_c^{(1)} = 25$, and $\zeta_c^{(2)} = 31.5$. For $\theta = \frac{\pi}{2}$ and $\beta = 50$, we have also found a triad of critical ζ values. Owing to the great amount of computation required, however, we did not attempt to map out the entire (β, θ) parameter space. Nevertheless, it is clear that end-pinching on a substrate is a complex and subtle phenomenon, with multiple transitions between breakup and complete retraction.

In view of the experimental focus on drop spacing, we have examined the center-to-center separation between the two daughter drops at $\zeta = \zeta_c$. At the critical filament length, the breakup leads to two drops for all cases, and thus we avoid the complication of the three-drop scenario. Figure 10 shows that the drop spacing decreases with increasing θ. In other words, if the filament wets the substrate poorly, the resultant drops will be closer. With hydrophobicity, the dewetting happens more rapidly and the tip retracts faster. At the same time, the necking also progresses at a faster pace, thus cutting down the time available for retraction. The first wins out in our simulations, leading to more closely spaced daughter drops.

At this point, it is interesting to compare the two types of capillary instabilities, growth of capillary waves and end-pinching. In both cases hydrophobicity hastens the growth of the instability and decreases the spacing between the neighboring droplets (see Figs. 4 and 10). These two phenomena

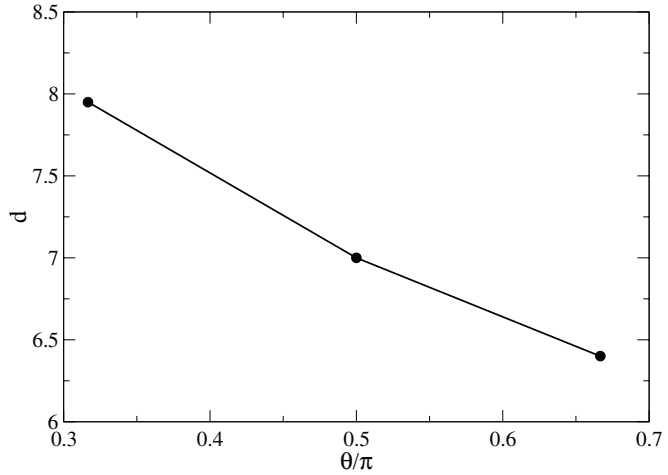

FIG. 10. The spacing between the two daughter drops decreases with increasing θ. $\beta = 10$ and ζ is at the critical ζ_c for each θ value.

also differ in several aspects. For example, capillary waves typically produce a secondary droplet between primary drops with a volume ranging from 1% to 5% (see Fig. 6), whereas in end-pinching, the secondary droplets are much smaller, with a volume ~0.1% of the whole strip, and are visible only at higher resolution ($Cn = 0.05$, not shown here). This can be understood by comparing Fig. 7 with Fig. 2. Since the end moves toward the center in end-pinching, the neck tends to be short. Thus, secondary necking takes place, if at all, close to the primary neck leaving only a small amount of fluid to form the secondary drop. Moreover, in our simulations the drop spacing is always somewhat smaller for end-pinching than for capillary wave breakup, by roughly 30%. A long filament may be susceptible to both breakup mechanisms with end-pinching close to the tips and the growth of capillary waves in the middle.

As our computation was partly motivated by end-pinching experiments, it is natural to compare the numerical results with the experiments. As is often the case,[4] quantitative comparison is hampered by limitations in the numerical or theoretical computation on the one hand and complexities in experimental conditions on the other. The former consists chiefly in our relatively short filaments that break up into only two or three droplets; on a long filament that undergoes multiple retraction and pinch-off cycles,[8] the drop spacing may be determined by somewhat different hydrodynamic factors. The latter includes contact angle hysteresis, asymmetric tip retraction, and possibly the simultaneous development of capillary-wave instability and end-pinching.[5,8,14] All conspire to produce non-spherical sessile drops that are polydisperse and non-uniformly spaced.

Subject to the above caveat, one experimental observation, that the daughter drops have tighter spacing on more hydrophobic surfaces,[8] has been successfully reproduced by the simulations. As noted above, this trend holds for both the capillary-wave instability and the end-pinching mechanism. For a more quantitative comparison, we take the experiment of Kondic *et al.*,[14] where they used laser pulses to melt two metallic strips (aspect ratio $\zeta = 412$ and 848, viscosity ratio $\beta \sim 250$) and then recorded their breakup. The measured retraction distance of the tips, after proper non-dimensionalization, is 10.6 and 8.1 for the two strips. Since the contact angle was not given, we infer $\theta \approx \frac{2\pi}{3}$ from their images, for which our end-pinching simulation predicts a retraction distance of 13 for the longest and most viscous filament computed ($\zeta = 38$, $\beta = 50$). Kondic *et al.*[14] also measured the distribution of drop spacings. In dimensionless terms, the spacing is 11 ± 5 and 13 ± 5 for the thicker ($\zeta = 412$) and thinner ($\zeta = 848$) strips. Though both breakup mechanisms are at work, their calculation showed that they should produce roughly the same spacing. Meanwhile, our simulations have predicted a spacing of 9.0 for capillary wave growth and 6.65 for end-pinching. These two values differ considerably, although both are on the same order of magnitude as the experimental values. As alluded to above, discrepancy in the drop spacing is not surprising. On a long filament, drops on either half have been formed during retraction in the same direction. On our short filament, the two drops are formed during retraction in opposite directions.

IV. CONCLUSION

We have presented a computational study of the two capillary instabilities that can break up a liquid filament on a substrate: the growth of capillary waves and end-pinching. Through three-dimensional simulations, we have characterized the effect of the contact angle and geometry of the filament on the development of the instabilities. In addition, we have investigated the effect of the viscosity contrast in the breakup by end-pinching of filaments of moderate length. The results differentiate these two phenomena for their dynamics and the configuration of the resultant daughter drops. For the parameter range tested, the results can be summarized as follows:

(a) For capillary waves the linear growth rate increases with the contact angle, while the fastest wavelength becomes shorter. Thus, hydrophobicity of the substrate facilitates the instability, and mostly through reduced viscous dissipation. This conclusion is consistent with existing theoretical, numerical, and experimental work.
(b) The final drop spacing always agrees with the wavelength of the fastest linear mode, although satellite drops tend to appear due to secondary necking before breakup.

(c) For end-pinching to occur, the filament has to have a length-to-diameter ratio above a critical value ζ_c that depends on the viscosity ratio and contact angle. In particular, ζ_c is lower for larger contact angle, so hydrophobicity again promotes breakup. Also, for all contact angles tested, ζ_c is 2 to 3 times smaller than that for a freely suspended filament.[32]
(d) The prediction that hydrophobicity promotes breakup and decreases the spacing of the daughter drops agrees qualitatively with experimental observations. This is true for both types of instability.

While the present study adds to our understanding of filament breakup, we have to underline its limitations. A generic and long-standing difficulty arises from the moving contact line. Our Cahn-Hilliard model may be more sophisticated than the various slip models, it is nevertheless phenomenological. Thus, the speed of retraction on a substrate, for one, cannot yet be predicted from first principles. On a more technical level, the 3D simulation of long filaments is computationally expensive, especially when high interfacial resolution is required. The demands of long computing time and large memory have restricted us to relatively short filaments. Thus, we cannot reproduce the complete end-pinching experiment that brings forth a large number of droplets along the filament. Experimental complexities such as contact angle hysteresis have been neglected as well. Obviously this seemingly simple process—breakup of an initially stationary liquid thread deposited on a solid substrate—requires still more research on both experimental and computational fronts.

ACKNOWLEDGMENTS

This research was partially supported by the NSERC, the Canada Research Chair program, and the Canada Foundation for Innovation. We acknowledge discussions with Professor Alejandro González, Professor Bud Homsy, and Professor Pengtao Yue.

[1] J. Eggers, "Nonlinear dynamics and breakup of free-surface flows," Rev. Mod. Phys. **69**, 865–929 (1997).
[2] S. H. Davis, "Moving contact lines and rivulet instabilities. Part 1. The static rivulet," J. Fluid Mech. **98**, 225–242 (1980).
[3] F. Brochard-Wyart and C. Redon, "Dynamics of liquid rim instabilities," Langmuir **8**, 2324–2329 (1992).
[4] L. Yang and G. M. Homsy, "Capillary instabilities of liquid films inside a wedge," Phys. Fluids **19**, 044101 (2007).
[5] Y. Wu, J. D. Fowlkes, P. D. Rack, J. A. Diez, and L. Kondic, "On the breakup of patterned nanoscale copper rings into droplets via pulsed-laser-induced dewetting: Competing liquid-phase instability and transport mechanisms," Langmuir **26**, 11972–11979 (2010).
[6] H. Stone, J. Bentley, and L. G. Leal, "An experimental study of transient effects in the breakup of viscous drops," J. Fluid Mech. **173**, 131–158 (1986).
[7] A. Y. Tong and Z. Wang, "Relaxation dynamics of a free elongated liquid ligament," Phys. Fluids **19**, 092101 (2007).
[8] A. G. González, J. Diez, R. Gratton, and J. Gomba, "Rupture of a fluid strip under partial wetting conditions," Europhys. Lett. **77**, 44001 (2007).
[9] M. S. McCallum, P. W. Voorhees, M. J. Miksis, S. H. Davis, and H. Wong, "Capillary instabilities in solid thin films: Lines," J. Appl. Phys. **79**, 7604–7611 (1996).
[10] J. A. Diez, A. G. González, and L. Kondic, "Stability of a finite-length rivulet under partial wetting conditions," J. Phys.: Conf. Ser. **166**, 012009 (2009).
[11] J. A. Diez, A. G. González, and L. Kondic, "On the breakup of fluid rivulets," Phys. Fluids **21**, 082105 (2009).
[12] J. A. Diez, A. G. González, and L. Kondic, "Instability of a transverse liquid rivulet on an inclined plane," Phys. Fluids **24**, 032104 (2012).
[13] T. D. Nguyen, M. Fuentes-Cabrera, J. Fowlkes, J. A. Diez, A. G. González, L. Kondic, and P. D. Rack, "Competition between collapse and breakup in nanometer-sized thin rings using molecular dynamics and continuum modeling," Langmuir **28**, 13960–13967 (2012).
[14] L. Kondic, J. A. Diez, P. D. Rack, Y. Guan, and J. D. Fowlkes, "Nanoparticle assembly via the dewetting of patterned thin metal lines: Understanding the instability mechanisms," Phys. Rev. E **79**, 026302 (2009).
[15] P. Yue, C. Zhou, J. J. Feng, C. F. Ollivier-Gooch, and H. H. Hu, "Phase-field simulations of interfacial dynamics in viscoelastic fluids using finite elements with adaptive meshing," J. Comput. Phys. **219**, 47–67 (2006).
[16] C. Zhou, P. Yue, J. J. Feng, C. F. Ollivier-Gooch, and H. Hu, "3D phase-field simulations of interfacial dynamics in Newtonian and viscoelastic fluids," J. Comput. Phys. **229**, 498–511 (2010).
[17] P. Yue, C. Zhou, and J. J. Feng, "Sharp-interface limit of the Cahn-Hilliard model for moving contact lines," J. Fluid Mech. **645**, 279–294 (2010).
[18] P. Yue, J. J. Feng, C. Liu, and J. Shen, "A diffuse-interface method for simulating two-phase flows of complex fluids," J. Fluid Mech. **515**, 293–317 (2004).
[19] J. W. Cahn, "Critical point wetting," J. Chem. Phys. **66**, 3667–3672 (1977).
[20] D. Jacqmin, "Contact-line dynamics of a diffuse fluid interface," J. Fluid Mech. **402**, 57–88 (2000).

[21] L. M. Pismen, "Nonlocal diffuse interface theory of thin films and the moving contact line," Phys. Rev. E **64**, 021603 (2001).
[22] L. M. Pismen, "Mesoscopic hydrodynamics of contact line motion," Colloids Surf., A **206**, 11–30 (2002).
[23] J. J. Feng, C. Liu, J. Shen, and P. Yue, "An energetic variational formulation with phase field methods for interfacial dynamics of complex fluids: Advantages and challenges," in *Modeling of Soft Matter*, edited by M.-C. T. Calderer and E. M. Terentjev (Springer, New York, 2005), pp. 1–26.
[24] P. Yue, J. J. Feng, C. Liu, and J. Shen, "Diffuse-interface simulations of drop coalescence and retraction in viscoelastic fluids," J. Non-Newtonian Fluid Mech. **129**, 163–176 (2005).
[25] P. Yue, C. Zhou, and J. J. Feng, "A computational study of the coalescence between a drop and an interface in Newtonian and viscoelastic fluids," Phys. Fluids **18**, 102102 (2006).
[26] J. J. Huang, C. Shu, and Y. T. Chew, "Mobility-dependent bifurcations in capillarity-driven two-phase fluid systems by using a lattice Boltzmann phase-field model," Int. J. Numer. Methods Fluids **60**, 203–225 (2009).
[27] P. Yue and J. J. Feng, "Wall energy relaxation in the Cahn-Hilliard model for moving contact lines," Phys. Fluids **23**, 012106 (2011).
[28] P. Yue and J. Feng, "Can diffuse-interface models quantitatively describe moving contact lines?" Eur. Phys. J. Spec. Top. **197**, 37–46 (2011).
[29] A. Zosel, "Studies of the wetting kinetics of liquid drops on solid surfaces," Colloid Polym. Sci. **271**, 680–687 (1993).
[30] J.-Y. Park, K. Y. Suh, S.-M. Seo, and H. H. Lee, "Anisotropic rupture of polymer strips driven by Rayleigh instability," J. Chem. Phys. **124**, 214710 (2006).
[31] J. Bostwick and P. Steen, "Stability of constrained cylindrical interfaces and the torus lift of Plateau-Rayleigh," J. Fluid Mech. **647**, 201–219 (2010).
[32] J.-W. Ha and L. G. Leal, "An experimental study of drop deformation and breakup in extensional flow at high capillary number," Phys. Fluids **13**, 1568–1576 (2001).